

# Leveraging Submarine DAS Arrays for Offshore Earthquake Early Warning: A Case Study in Monterey Bay, California

Yuancong Gou<sup>\*1</sup>, Richard M. Allen<sup>1</sup>, Weiqiang Zhu<sup>1</sup>, Taka'aki Taira<sup>1</sup>, and Li-Wei Chen<sup>1,2</sup>

## ABSTRACT

Detecting offshore earthquakes in real time is challenging for traditional land-based seismic networks due to insufficient station coverage. Application of distributed acoustic sensing (DAS) to submarine cables has the potential to extend the reach of seismic networks and thereby improve real-time earthquake detection and earthquake early warning (EEW). We present a complete workflow of a modified point-source EEW algorithm, which includes a machine-learning-based model for *P*- and *S*-wave phase picking, a grid-search location method, and a locally calibrated empirical magnitude estimation equation. Examples are shown with offshore earthquakes from the SeaFOAM DAS project using a 52-km-long submarine cable in Monterey Bay, California, demonstrating the robustness of the proposed workflow. When comparing to the current onshore network, we can expect up to 6 s additional warning time for earthquakes in the offshore San Gregorio fault zone, representing a substantial improvement to the existing ShakeAlert EEW system.

## KEY POINTS

- A workflow is developed using a seafloor distributed acoustic sensing (DAS) array for earthquake early warning.
- Examples of earthquake detection are shown with the DAS data from offshore events in Monterey Bay, California.
- Estimation of additional warning time up to 6 s can be gained for the offshore San Gregorio fault zone.

## Supplemental Material

## INTRODUCTION

Earthquake early warning (EEW), which provides seconds to tens of seconds of warning for potentially damaging earthquakes, has been developed and is operational in many regions worldwide (Allen and Melgar, 2019). Effective EEW systems depend heavily on dense seismic networks. However, the greatest earthquake risks are often found in offshore regions, which lie beyond the coverage of most land-based seismic networks. It has always been a challenge to detect and characterize events that occur outside of the network in EEW systems (Netanel *et al.*, 2021; Ziv *et al.*, 2024). Lack of near-source triggers leads to longer detection delays. Lack of azimuthal coverage leads to poorly constrained earthquake locations, which consequently introduces errors in the magnitude estimation. For example, Williamson *et al.* (2023) found that insufficient network coverage is responsible for inaccurate characterization of offshore events in the Mendocino triple

junction. Some earthquake-prone countries adjacent to subduction zones have made significant efforts to increase offshore seismic observations by building cabled ocean-bottom seismometer (OBS) networks such as S-Net in Japan (Kanazawa *et al.*, 2016). The costs of real-time OBS networks are very high, and the network is difficult to maintain.

Recent advances in distributed acoustic sensing (DAS) reveal the optical fiber sensing technology's potential in ocean-bottom seismic monitoring. DAS could provide axial strain measurements along fiber-optic cables by sensing optoelectronic signals, through an interrogator unit connected to one end of the cable (Zhan, 2020; Lindsey and Martin, 2021). Applying DAS to existing submarine cables has been demonstrated to be effective in detecting earthquakes and ambient seismic field and oceanic signals (Lindsey *et al.*, 2019; Sladen *et al.*, 2019; Cheng *et al.*, 2021; Lior, Sladen, *et al.*, 2021; Matsumoto *et al.*, 2021; Williams *et al.*, 2023; Xiao *et al.*, 2024). Many studies have explored the feasibility of using DAS data for real-time

1. UC Berkeley Seismological Laboratory (UCB), Berkeley, California, U.S.A., <https://orcid.org/0000-0001-6313-0564> (YG); <https://orcid.org/0000-0003-4293-9772> (RMA); <https://orcid.org/0000-0003-2889-1493> (WZ); <https://orcid.org/0000-0002-6170-797X> (TT); <https://orcid.org/0000-0002-9403-4505> (L-WC);

2. Lawrence Berkeley National Laboratory, Berkeley, California, U.S.A.

\*Corresponding author: yuancong\_gou@berkeley.edu

**Cite this article as** Gou, Y., R. M. Allen, W. Zhu, T. Taira, and L.-W. Chen (2025). Leveraging Submarine DAS Arrays for Offshore Earthquake Early Warning: A Case Study in Monterey Bay, California, *Bull. Seismol. Soc. Am.* **115**, 516–532, doi: [10.1785/0120240234](https://doi.org/10.1785/0120240234)

© Seismological Society of America

earthquake detection (Farghal *et al.*, 2022). For example, Yin, Soto, *et al.* (2023) showed examples directly using DAS data offshore Chile to detect nearby events and its potential benefits for an EEW system; Lior *et al.* (2023) explored the potential using ground-motion data converted from DAS data to estimate earthquake magnitude.

During the pilot study by Lindsey *et al.* (2019), DAS was applied to a submarine cable in the Monterey Accelerated Research System (MARS, we will refer to the cable as MARS cable in this article), a cabled observatory owned by Monterey Bay Aquarium Research Institute (MBARI). In 2022, we started the SeaFOAM (The Seafloor Fiber-Optic Array in Monterey Bay) project (Romanowicz *et al.*, 2023) using the same MARS cable funded by the National Science Foundation (NSF). After the originally proposed one year duration, the project was extended to be a permanent deployment with support from the CalOES (California Governor's Office of Emergency Services). Considering the offshore seismic hazards and the limitations of on-land seismic networks discussed earlier, we aim to use real-time DAS data to enhance EEW and monitor the seismic activity in this region, with a special focus on offshore faults.

In California, several offshore faults have hosted large historical earthquakes and have the potential for big earthquakes in the future (Field *et al.*, 2015). Paleoseismology, seafloor geomorphology, multibeam surveys, and active-source reflection seismology are most commonly used to map and study these offshore faults, which are generally less constrained compared to their on-land neighbors. The earthquake hazards associated with these offshore faults are not negligible, extending all the way from the Mendocino triple junction in Northern California down to offshore Los Angeles. The 1906 San Francisco earthquake is believed to have originated from the offshore section of the San Andreas fault (SAF; Lomax, 2005). The San Gregorio fault (SGF) is an offshore fault extending from the southern reaches of Monterey Bay to Bolinas Bay, northwest of San Francisco, where it intersects with the SAF (Graham and Dickinson, 1978). Paleoseismic evidence from trenches on the SGF's intersection with the San Francisco Peninsula suggests it has experienced an  $M$  7+ event after A.D. 1270 (Simpson *et al.*, 1997). More recently, Johnson *et al.* (2018) discussed the potential seismic hazards of a connected San Gregorio-Hosgri fault system, which could be ruptured during one single event through the Big Sur Bend. The estimated earthquake magnitude in this scenario is  $M$  7.8, and the strong shaking could also trigger coastal landslides and tsunamis. The largest earthquake ever recorded by modern instruments on the SGF was  $M$  6.4 in 1926, located inside the Monterey Bay according to the International Seismological Centre-Global Earthquake Model (ISC-GEM) Catalog (Di Giacomo *et al.*, 2018).

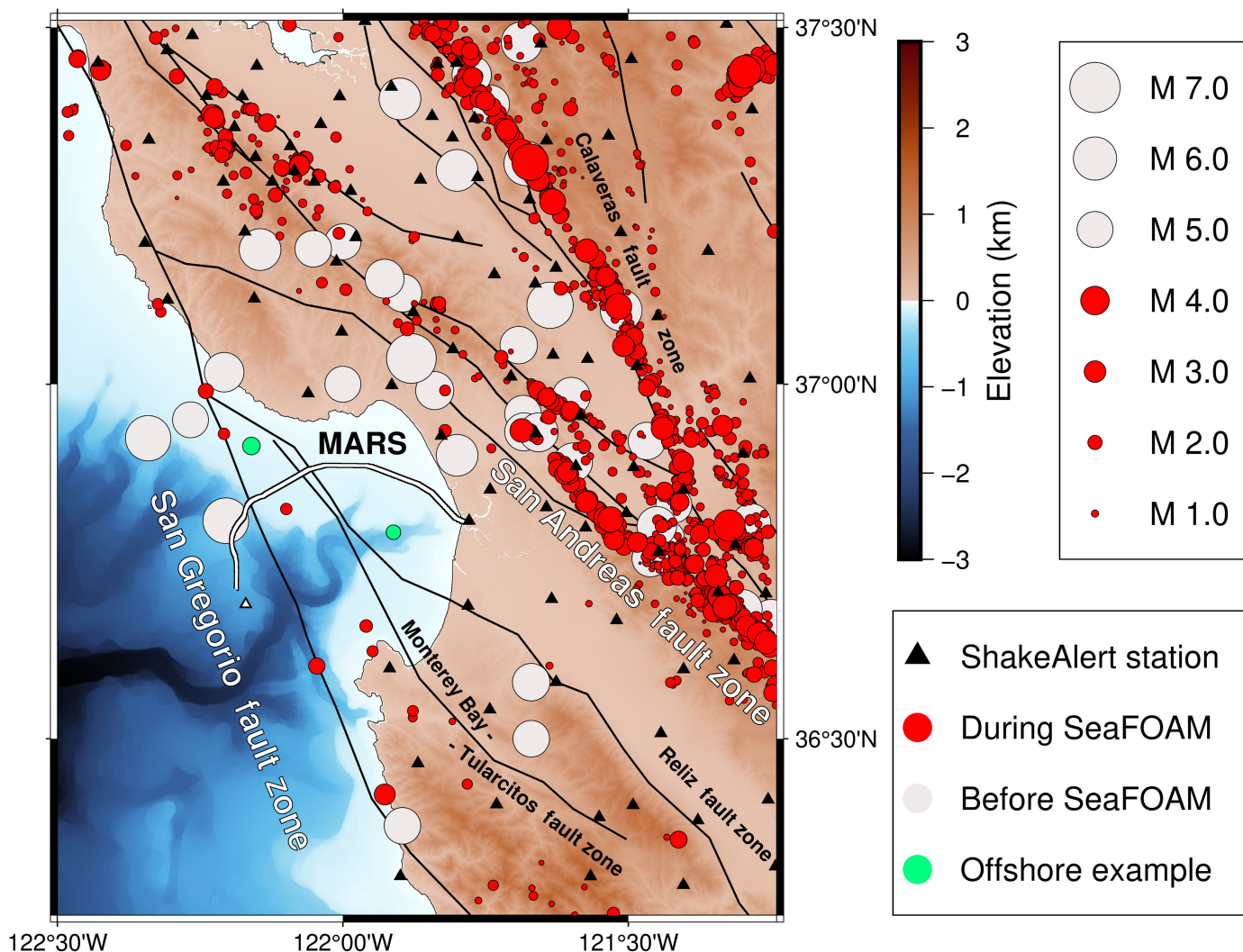
Some significant historical earthquakes with magnitudes larger than 5 are shown in Figure 1, including the 1989  $M$  6.9 Loma Prieta earthquake on the SAF north of Monterey Bay. The

SGF is still geologically active with a modern slip rate less than 10 mm/yr (Wills *et al.*, 2007). A few studies reveal complex sub-fault systems in the Monterey Bay, including potentially unmapped faults found by Lindsey *et al.* (2019). One of the first broadband OBSs named Monterey Ocean Bottom Broadband (MOBB) observatory was deployed in Monterey Bay and was contributing data to the Berkeley seismic network from 2003 (Romanowicz *et al.*, 2003). MOBB contributed to the detection of many offshore events inside Monterey Bay as the closest station, before it was unfortunately shut down by a trawling event in 2016. Seismic hazard models rely on seismicity, slip rate, and other information to forecast earthquakes on faults. Therefore, more seismic observations offshore could improve seismic hazard forecasting on the SGF.

Given the historical seismicity and recent research on the current SGF, it is evident that the offshore seismic hazard poses a notable concern. However, there are significantly fewer instruments available to provide timely detection for EEW in this offshore region, especially when comparing to the density of stations on land. Figure 1 shows all the seismic stations that are currently contributing to the ShakeAlert (Kohler *et al.*, 2020) EEW system for the west coast of the United States. Since the public rollout, ShakeAlert has issued numerous widely distributed public alerts in California (Lux *et al.*, 2024). One of the main EEW algorithms featured in ShakeAlert is EPIC (Earthquake Point-source Integrated Code), which is a point-source EEW algorithm that detects earthquakes using  $P$ -wave arrivals close to the epicenter to locate the earthquake and estimate the magnitude, based on the point-source assumption and local velocity models (Chung *et al.*, 2019). EPIC has been intensively evaluated and verified as a timely and robust EEW algorithm. The operational principles of EPIC necessitate a dense network coverage over the region of interest, thus integrating DAS data to EPIC could help improve EEW for offshore events. In this article, we present a complete workflow to utilize DAS data from the SeaFOAM project for earthquake detection in real time for the purpose of EEW, demonstrating procedures including seismic arrival triggering, earthquake location, and magnitude estimation.

## SeaFOAM DAS DATA

An OptaSense DAS interrogator (model QuantX) has been connected to the 52-km-long MARS cable since the start of SeaFOAM in July 2022. As of 16 November 2024, continuous data have been recorded for 840 days, with a data completeness rate of 98.7%. Data gaps are due to a few interruptions from power outages and maintenance. Details about the data acquisition process can be found in Romanowicz *et al.* (2023). Raw data were collected with a 200 Hz sampling rate, 20.4 m gauge length, and 5.1 m channel spacing, which can be proportionally converted to strain. We obtained 10,245 channels with this configuration.



Getting accurate location information of existing DAS cables has always been a challenge for the seismology community. When the information is not provided by the owner, people usually interpolate locations of control points along the cable obtained by “tap” test or moving vehicles (Biondi *et al.*, 2023) to get the location of each DAS channel. For submarine cables, the lack of accessibility makes the channel locating task more difficult. Collaboration with MBARI allows us to take advantage of their cable inspection report for detailed cable conditions. MBARI conducts repeated surveys on the MARS cable every five years to inspect the cable’s condition and potential environmental effects, using a Remote Operating Vehicle (ROV). The ROV records high-quality video footage at control points from which we can observe the cable’s substrate composition, coupling condition, and forced movement. The most recent survey (Kuhnz *et al.*, 2020) was conducted in 2020. The report includes the cable’s burial condition, points of suspension, and spans due to steep bathymetry. As shown in Romanowicz *et al.* (2023), the background noise level of the DAS channels along the cable correlates well with bathymetry and substrate composition.

**Figure 1.** Recent and historical seismicity near Monterey Bay, California. The white line extending across the bay represents the Monterey Accelerated Research System (MARS) cable used in this study. Circles represent earthquake epicenters, with their sizes proportional to the magnitude. Red circles are earthquakes of all magnitude during the SeaFOAM project (until the draft of this article in April 2024) from the U.S. Geological Survey (USGS) ComCat catalog. Gray circles are historical earthquakes with magnitude larger than 5 from the International Seismological Centre-Global Earthquake Model (ISC-GEM) Catalog. The green circles are two offshore earthquakes later discussed in this study as examples of event detection using distributed acoustic sensing (DAS). Black triangles represent seismic stations currently used by the ShakeAlert system. The white triangle is the offshore station MOBB. Fault lines are shown in black. The color version of this figure is available only in the electronic edition.

Because we aim to develop methods using DAS arrays to detect earthquakes, we first need a data set that contains recorded earthquake waveforms. Our earthquake data set preparation process follows that outlined by Zhu *et al.* (2023). We cut 120-s-long waveforms containing the earthquake from the continuous data using an approximate estimation of P-wave arrival times for local U.S. Geological Survey (USGS)

catalog events between August 2022 and April 2023. We preserve the HDF5 data format and DAS acquisition parameters such as gauge length and channel spacing from continuous data. Then, we added reformatted metadata such as earthquake source parameters, event ID, and start and end time. The estimated first  $P$ -wave arrival at the DAS array is placed around 30 s into the data window. This resulted in 311 events with good signal-to-noise ratios (SNR), which we will be using both in the machine learning (ML) training process and magnitude calibration process discussed later.

## EARTHQUAKE DETECTION METHODS

A complete workflow for a point-source-based EEW system includes detecting seismic arrivals (real-time phase picking), earthquake location, magnitude estimation, ground-motion prediction, and alert distribution, which should all be finished in a sequential and timely fashion. The goal of the first three steps is to obtain earthquake source parameters, which will be the focus of this study. To facilitate integration to the existing ShakeAlert EPIC algorithm in the future, while also exploring the full potential of a dense DAS array, we developed an algorithm that is consistent and compatible with EPIC workflow (Chung *et al.*, 2019).

### Detecting seismic arrivals

Accurate detection of seismic arrivals is the first and an essential step of the workflow because it directly affects the following processes of earthquake location (Bozzi *et al.*, 2024) and magnitude estimation. Traditional seismic arrival picking methods based on single station data are not well suited for DAS data for several limitations for a few reasons: (1) the dense spatial information provided by the DAS array is underutilized; (2) determining optimal parameters is challenging due to different background noise levels across a large number of channels; (3) methods that require three-component data are not directly applicable. For example, short-term average/long-term average method (Allen, 1982) may require fine-tuning for each DAS channel to determine the best-window lengths and thresholds, since strain or strain-rate data recorded by DAS will amplify scatter waves, which will make picking  $P$ - and  $S$ -wave arrivals challenging (Capdeville and Sladen, 2024).

Here, we applied an ML method for seismic phase picking. The ML model was trained using a semi-supervised transfer-learning approach based on PhaseNet-DAS (Zhu *et al.*, 2023). The original PhaseNet-DAS model has a U-net structure inherited from PhaseNet (Zhu and Beroza, 2019), which is a single-station-based seismic phase-picking model. PhaseNet-DAS was modified to take a 2D input (time and space domain) of DAS data and was trained using a data set consisting of onshore DAS data.

Directly applying the original model to events from the SeaFOAM data set gave suboptimal results for some parts of the cable. The issues included picking phases discontinuously

across the DAS array and misidentification of phase types. Because of the “uninterpretable” nature of neural networks (LeCun *et al.*, 2015), we cannot be certain of the exact causes, but we can speculate on the reasons for the reduced performance:

1. DAS data are known to exhibit different background noise levels because of its broadband observation ability (Lindsey *et al.*, 2020) and variability in cable coupling conditions (Reinsch *et al.*, 2017; Hudson *et al.*, 2024). Submarine DAS arrays can record both seismic and oceanic waves (Lindsey *et al.*, 2019; Sladen *et al.*, 2019; Lior, Sladen, *et al.*, 2021); therefore, they must be explored separately from on-land DAS arrays. One can easily see the differences when looking at raw recordings and power spectral density analysis. Supervised or semi-supervised ML models rely heavily on training data and may not generalize well to new data sets. In this case, it is reasonable that the original PhaseNet-DAS model, trained with onshore data, does not work as well for submarine DAS data.
2. Interrogators may have different measuring techniques. Depending on the needs, different choices for parameters such as gauge length, channel spacing, and the choice between strain or strain-rate outputs are made for individual DAS deployments. An obvious consequence is the amplification of high-frequency signals in strain-rate data than strain data. Currently, the community is still working toward standards for DAS data acquisition (Hui Lai *et al.*, 2024). The original PhaseNet-DAS model was trained on 100 Hz strain-rate data with  $\sim 10$  m channel spacing. The SeaFOAM project operates with  $\sim 5$  m channel spacing to record 200 Hz strain data. The different sampling choices may affect the “sense” of time and space of the ML model because the convolution kernels may be trained to interpret DAS data at a certain scale.

Given these concerns, and the tests on real SeaFOAM data, we decided that the original PhaseNet-DAS model was not suitable for direct application to the SeaFOAM data set. We instead took a transfer-learning approach that is commonly used in the ML community to get an improved model starting with a more generic original model. The new model preserves the main features from the original model but performs better with the DAS data collected in submarine environments.

### Transfer learning of PhaseNet-DAS model

The semi-supervised transfer-learning approach has a workflow similar to the original PhaseNet-DAS model (Fig. 2).

1. We first applied the original model to the earthquake data set from SeaFOAM (as described in the [SeaFOAM DAS Data](#) section) to prepare labels for the training process. The labels mark DAS data points as  $P$ -,  $S$ -wave arrivals, or noise. Then, we trained a new model using data with

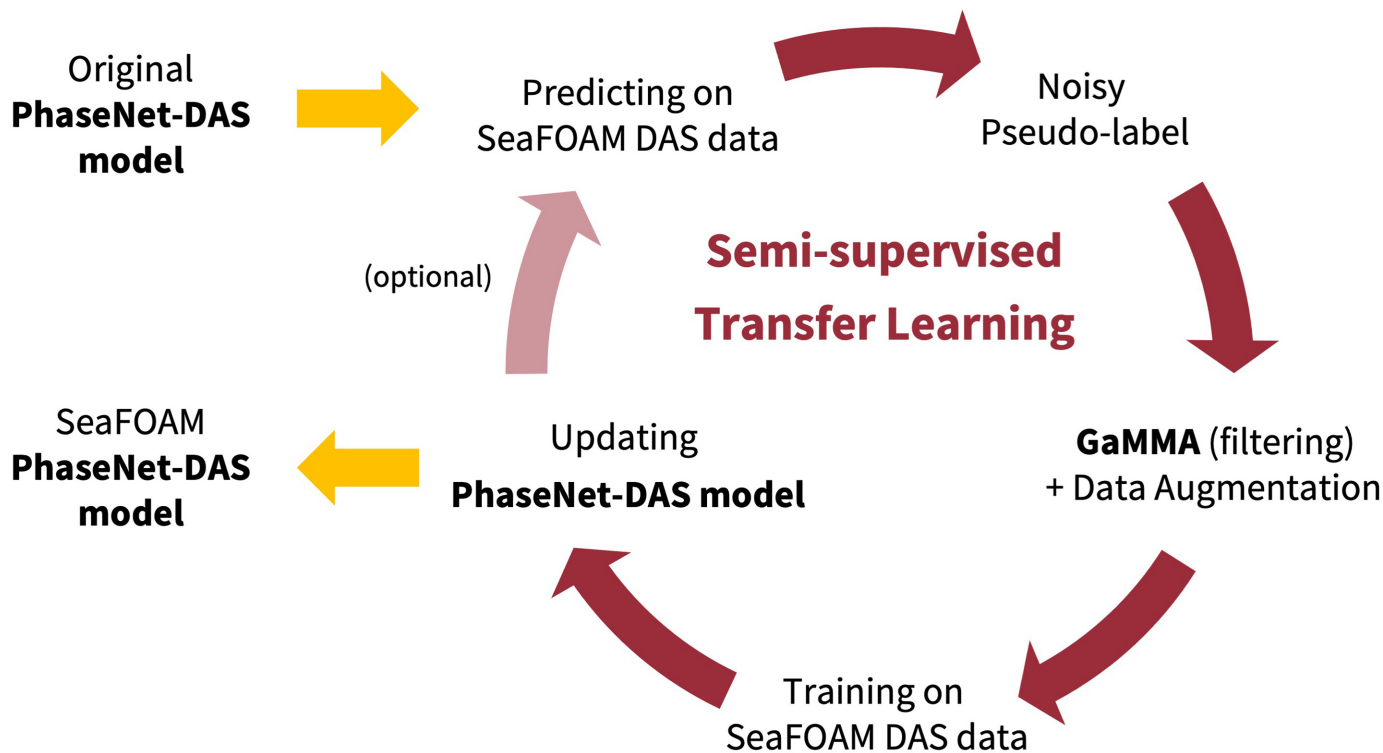


**Figure 2.** Transfer-learning workflow. The original PhaseNet-DAS model (Zhu *et al.*, 2023) is applied to new data from SeaFOAM to generate noisy pseudo labels, which are then filtered by the association algorithm GaMMA (Zhu *et al.*, 2022) for training. It is optional to repeat this semisupervised process. The details are explained in the [Transfer learning of PhaseNet-DAS model](#) section. The color version of this figure is available only in the electronic edition.

SeaFOAM DAS configuration (200 Hz, ~5 m). To generate labels for training, we needed to apply the original model with the original configuration (i.e., 100 Hz, ~10 m). Therefore, we initially applied decimation to the data both in time and space domain to roughly match the 100 Hz, ~10 m sampling rates of the data that the original model was trained on. After we applied the original model to the decimated data, we obtained noisy pseudo labels. They are called “noisy pseudo labels,” which also contain false picks for *P* and *S* arrivals.

2. The noisy pseudo labels generated in step 1 were filtered out using an earthquake association algorithm, the Gaussian Mixture Model Association (GaMMA) (Zhu *et al.*, 2022). GaMMA was designed to handle a large number of picks, for example from ML phase pickers. It serves as a filter to exclude false labels for outputs from the original PhaseNet-DAS model. We used a constant *P*-wave velocity of 5.6 km/s, *S*-wave velocity of 3.2 km/s in GaMMA to associate the picks. The choice of *P*-wave velocity is an average apparent velocity for some local earthquakes, which were recorded on traditional seismic station MOBB near the end of the cable with reasonable seismic wave speeds, whereas scattered false picks with large offsets were filtered out.
3. Manual inspection was then performed on the picks associated by GaMMA before they were used as labels in training. As aforementioned, the filtering process by GaMMA did not guarantee the associated picks were all correct and had good SNR. Manual inspection in the first iteration of this transfer learning approach was necessary for the

- small data set used for transfer learning. We wanted to keep only very good quality training data to tune the model without making the training task too challenging at first. After the first iteration, we could use the new model to repeat this process where we could loosen the criteria to include more picks as labels. Examples of final training data are shown in Figure S1, available in the supplemental material to this article. Although the labels were prepared on 100 Hz and 10 m data, we then used the SeaFOAM’s data without decimation (200 Hz, 5 m) in the training process (Fig. S1). After this step, we had 311 events with good *P*- and *S*-wave picks.
4. We split the prepared data set into a training and a testing data set with a ratio of 8:2, which contains 248 and 63 events, respectively. Because most of the phase arrival labels were generated on data with good SNR, and we also wanted the new model to generalize to noisy data, similar data augmentation methods (randomly flipping data along the spatial axis, masking part of data, superimposing double events, and stretching [resampling] along the temporal and spatial axes) as used in Zhu *et al.* (2023) were applied to the training data set. In addition, we also randomly selected around 300 data segments containing only noise (120-s-long data

without any signals from earthquakes) from the period August 2022 to April 2023. These noise segments were randomly stacked (superimposed) with the training data to enhance the training. A more detailed description of these training processes can be found in the supplemental material including loss during the training process (Figs. S2, S3). The new model was trained for 100 epochs on two Tesla T4 graphics processing units (GPUs) in Berkeley Seismological Lab (BSL).

### Comparison between the original PhaseNet-DAS model and new models

Examples of phase-picking performance comparison between the original PhaseNet-DAS model and new model are shown in Figure 3. We can see the improvement in phase-picking continuity and accuracy, which is even more obvious when applying the model to data in moving windows to simulate a real-time situation. To further evaluate the models trained using the semi-supervised method, we need quantitative analysis of the model performances. Just like for any other ML models for seismic phase picking, ground-truth data are difficult to define or obtain. People generally approach this problem by (1) comparing to manual phase picks, (2) comparing to theoretical arrivals from a velocity model, and (3) comparing relative arrival-time differences using cross correlation.

There are multiple challenges in the case of this data set. Manual labels for DAS data are not realistic due to the large data volume. The recorded earthquake wavefields in SeaFOAM data are complicated. DAS is proven to be sensitive to small-scale local heterogeneity (Singh *et al.*, 2020; Capdeville and Sladen, 2024), which will potentially lower the SNR for *P*- and *S*-wave arrivals. We also have observed effects due to underwater basin resonance (Lior *et al.*, 2022) and scattered waves from fault zones (Atterholt *et al.*, 2022; Yang *et al.*, 2022), which might impair the detection of *P*- and *S*-wave arrivals. Finally, it is difficult to calculate accurate theoretical arrivals simply using a 1D velocity model. Because of these reasons, the original PhaseNet-DAS model was evaluated using the cross-correlation method. Here, we focus on a direct comparison between new models and the original model. We therefore defined metrics to evaluate a model's phase detection ability considering both the DAS array as a whole and each channel individually. The metrics include numbers of events that had more than 2000 *P* or *S* arrival picks (~20% of all channels), numbers of events that were associated by GaMMA, mean *P* or *S* phase scores (the quality metric assigned to each pick by the ML model), average number of *P* or *S* arrivals per event, and mean *P*-wave detection gap (sections along the cable that did not have continuous picks). Detailed explanations can be found in Tables S1 and S2. The new SeaFOAM-PhaseNet-DAS performed better overall according to these metrics and was used in the next steps.

### Grid-search EEW earthquake location method

We used a grid-search method to find the earthquake location with minimum *P*-arrival time misfit to theoretical arrival times from a 1D seismic velocity model. The workflow steps were as follows.

1. We used a local 1D velocity model for Monterey Bay and nearby regions (Begnaud *et al.*, 2000) to calculate theoretical first *P*- and *S*-travel time from 0 to 300 km epicentral distances for an earthquake depth of 6.5 km (average earthquake depth in this region).
2. We discretized a rectangular search region centered around the DAS array (36.25° N, 37.51° N, 121.24° W, 122.50° W) with 0.02° grid spacing.
3. We calculated the theoretical arrival times for all DAS channels from each grid point (representing all possible earthquake locations in the grid search).
4. When the ML model outputs phase picks from the moving window scrolling through the DAS data, we use the *P*-arrival picks and the precalculated arrival times to evaluate the misfit for all possible earthquake locations. When a channel had both *P*- and *S*-arrival picks available, we also calculated (*S*-*P*) time and compared to precalculated (*S*-*P*) arrival times in the same way.
5. The misfits were weighted using different metrics and converted into likelihoods. For the conversion, we calculate the inverse of the misfit at each grid point, and the "likelihood" is determined by normalizing this value against the total sum of the inverse misfits across all grid points. The output picks from the ML model include a quality metric that ranges from 0 to 1 for each pick. The arrival-time misfit at each available channel was multiplied by the inverse of this quality metric. Then, this weighted misfit was converted into a likelihood between 0 and 1. The resultant likelihood was then multiplied by the ratio of the number of available channels to the number of total channels. The weighted likelihood calculated for all *P* arrivals was finally multiplied by likelihood from the (*S*-*P*) time when available.
6. If the event grid location with highest likelihood exceeded a given threshold, the algorithm declares that an event is detected at that location. As more information (higher quality picks and larger numbers of picks) becomes available over time, the likelihood distribution for each sequential step is multiplied recursively. The location is updated at each chosen timestep (every 0.16 s). The recursive process ensures that the location does not solely rely on the *P*- and *S*-arrival picks from a certain time window, which has a finite length and may contain incomplete wavefields in real time.
7. When the number of grid points with high likelihood (top 30th percentile) is less than 9, we assume the location result has converged. To prevent low nonnormalized likelihood from vanishing in the recursive multiplication, which might

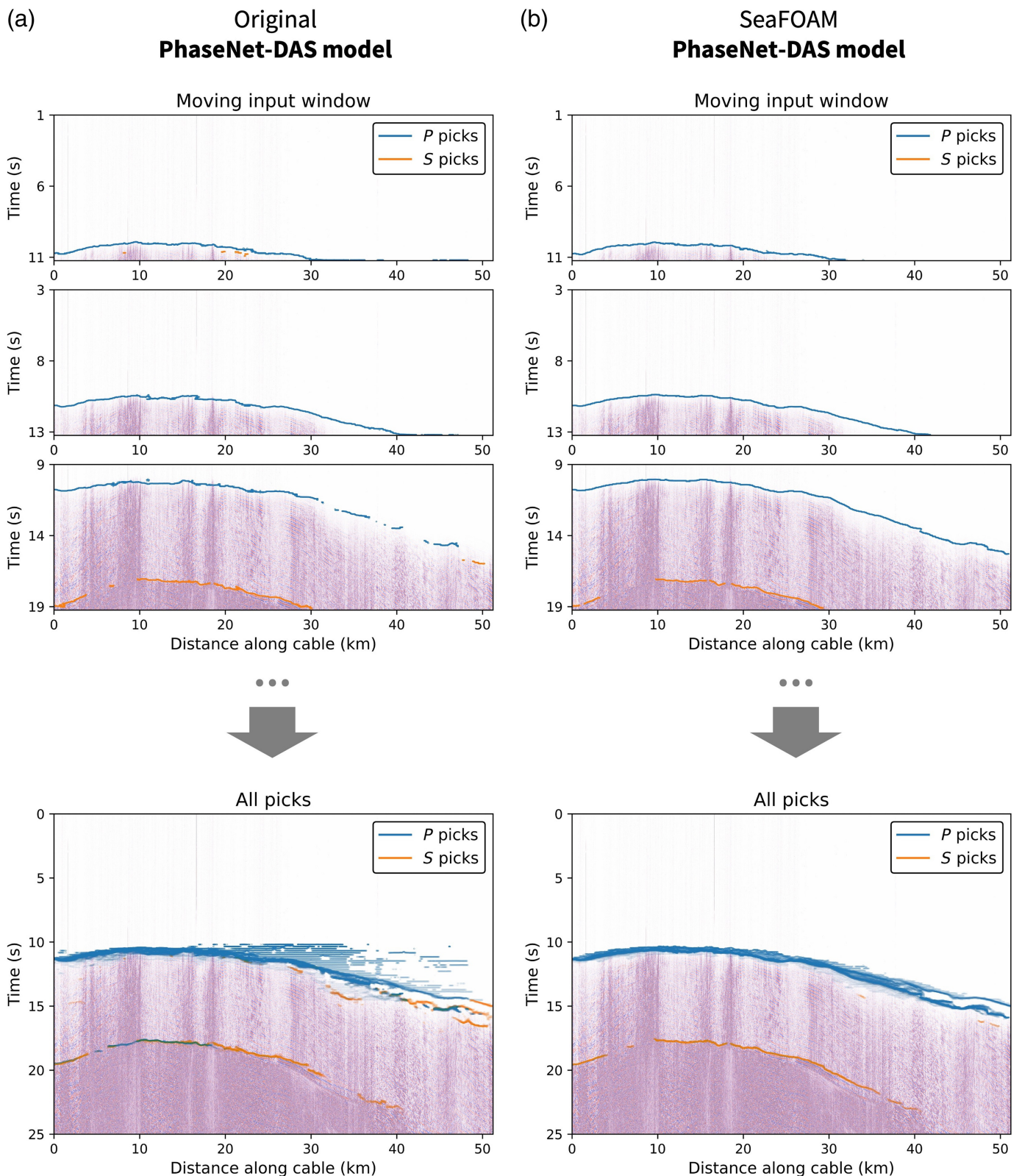
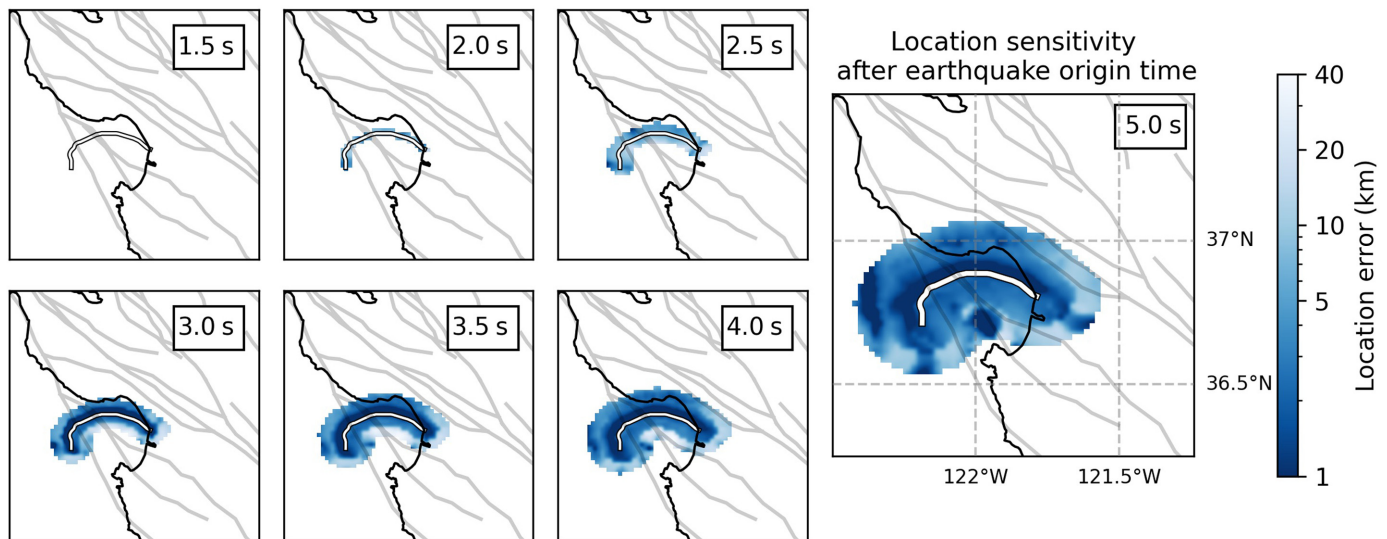


**Figure 3.** Performance comparison for the original PhaseNet-DAS model and the SeaFOAM-PhaseNet-DAS model for an **M** 5.1 event. The machine learning (ML) models are applied to 0.5 Hz high-pass filtered strain-rate data in  $\sim 10$ -s-long moving windows. (a) Results using the original model and (b) new SeaFOAM model. Upper panels show snapshots of the picking results for three time windows, whereas the lower panels show all the *P* and

*S* arrivals that were picked and the model scrolls through the input data. The picks are shown in darker color for earlier windows to show the picking performance when the arrivals first appear at the edge of the windows. Note that later picks overlap with each other, so the most commonly picked points will also appear darker. The color version of this figure is available only in the electronic edition.



cause problems in calculation, we rescaled the location result by normalizing the highest likelihood to 1 to stabilize the location process.

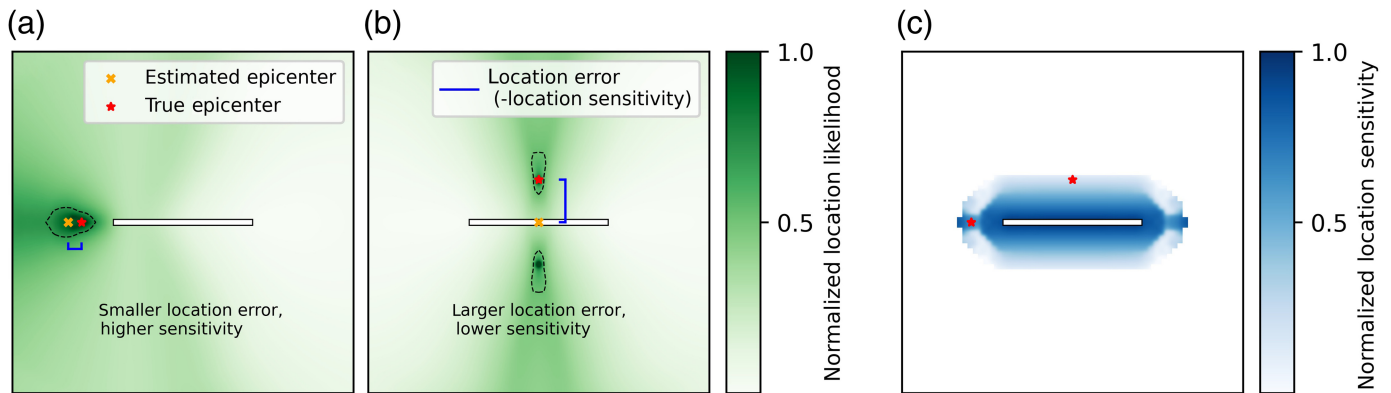
The principal concept underlying this method is the comparison of the moveout curve observed on the DAS array to theoretical predictions from a 1D velocity model to constrain the back azimuth. In addition, we use differential arrival time between *S* and *P* phases (when available) to constrain the distance to the event. Using a 1D velocity model was straightforward to implement and we expect that theoretical arrival times with a 1D velocity model would be accurate enough for EEW purposes. Local velocity variation and scattering effects can be observed in the data but they do not change the overall moveout curve significantly across the DAS array. It should be noted that the method does not search for origin time of the earthquake, which saves computational time (Yin, Soto, *et al.*, 2023) and focuses on relative arrival times to estimate event locations. To measure misfits between theoretical and observed moveouts, we aligned the first *P* arrival detected among observed DAS data to theoretical moveout data. The weighting scheme in this method takes full advantage of the PhaseNet-DAS model and dense array observation from DAS. The use of number of picks and phase scores as weights reduces the effect of low-quality picks from the ML model. The ratio of triggered channels to total channels provides higher weights when more channels have picks in the recursive location process. It also prevents triggering only on some parts of the cable due to local disturbances with fewer subsequent picks. Once we have an estimated epicenter, we use the theoretical travel time from that location to the DAS array to shift the arrival time observed on each channel to get the earthquake origin time. The median results from all channels will be used as the estimated earthquake origin time (Yin, Soto, *et al.*, 2023). Finally, our approach is principally similar to EPIC, which means it will be relatively straightforward to integrate into EPIC in the future.

**Figure 4.** Time-dependent location sensitivity. The location sensitivity is quantified in terms of the location error (in kilometers). The sensitivity is a function of time after the earthquake origin time and is shown for various points in time. The color version of this figure is available only in the electronic edition.

### Location error estimation and sensitivity

We estimate the error in location, and explore the sensitivity of a DAS cable to earthquakes at various locations, by considering the theoretical phase arrival times at the DAS cable for earthquakes at all possible locations. Figure 4 shows the time-dependent location sensitivity for the DAS cable. We start at zero time (the origin time of the earthquake). For every possible earthquake location, we determine which phases will have arrived at which DAS channel locations. At 1.5 s after the origin time (first panel in Fig. 4), there are no arrivals from any of the possible earthquake locations (the earthquake depth is at 6.5 km). Because we march forward in time, *P* waves (and *S* waves) arrive at the channels closest to the cable so there is sensitivity to earthquake locations closest to the fiber. As time progresses, the cable is sensitive to earthquakes at greater distances. At 5.0 s, the fiber is capable of detecting earthquakes from anywhere in Monterey Bay.

The details of how these sensitivities are calculated are illustrated in Figure 5. At each point in time, and for every possible candidate earthquake location, we calculate which phases have arrived at which DAS channels. Based on the arrival times, we can do a grid search to find the best-fit earthquake locations using the misfit of the actual arrival times to the expected arrival times for every possible earthquake location. This is illustrated in Figure 5a,b. The true earthquake location is shown as a red star, the green indicates how well all possible earthquake source locations fit the arrival times for the true location. We then select the most likely candidate locations (the top 0.3rd percentile; dashed lines in Fig. 5a,b), and



determine the centroid of these candidate locations (yellow cross). The location error is then the distance between the true and centroid locations. We take the negative of this distance as the location sensitivity and normalize it between 0 and 1 in Figure 5c. In this sensitivity test, it is important to quantify location error uniformly. While it is challenging for multimodal distributions as shown in Figure 5b, using the average error, such as in the two local maxima case, is reasonable. In this linear array setup, the algorithm will select a single best location, placing it either on the correct side or the opposite. The mean distance effectively represents the average location error.

Returning to the true DAS cable scenario shown in Figure 4, we can see expected variations in location sensitivity based on the geometry of the cable. There is greater sensitivity to location immediately north of the cable because the cable is curved to the south. The cable clearly has sensitivity throughout Monterey Bay including locations along the SGF.

### Magnitude estimation using an empirical scaling law

Most of the DAS interrogators record strain or strain-rate data translated from optical signals. Studies using DAS data to estimate earthquake magnitude for the purpose of EEW can be divided into two main categories. (1) Magnitude is estimated directly from strain or strain rate; (2) strain or strain-rate data are converted into ground-motion data (displacement, velocity, or acceleration) first, and then used to estimate magnitude. Taking the first approach requires empirical relationships derived based on strainmeters data or DAS data to determine magnitude. This includes using magnitude scale for local earthquakes based on broadband dynamic strain waveforms recorded on strainmeters (Barbour *et al.*, 2021), using relative magnitude calibration with reference data from seismometers (Li *et al.*, 2021) and deriving a new scaling law among peak strain rate, distance, and magnitude from a large data set (Yin, Zhu, *et al.*, 2023). For the second approach, once strain or strain-rate data are converted to ground-motion data, existing methods can be applied. For example, Lior, Sladen, *et al.* (2021) accomplishing this conversion in real time using slant-stack and estimating magnitude by fitting earthquake source model; Trabattoni *et al.* (2023) developed methods

**Figure 5.** Illustration of location sensitivity determination. A straight cable is used to demonstrate the calculation of location sensitivity. Panels (a) and (b) illustrate two misfit functions for two different earthquake locations (red cross) calculated at a specific point in time. The location error is the distance between the true earthquake location and the centroid (yellow cross) of the most likely 0.3rd percentile locations (dashed line). The location sensitivity is quantified as the distance or location error between the true epicenter and the estimated epicenter. (c) The location sensitivity calculated for all candidate earthquake locations at a given point in time. The two example earthquake locations are shown as red stars. The color version of this figure is available only in the electronic edition.

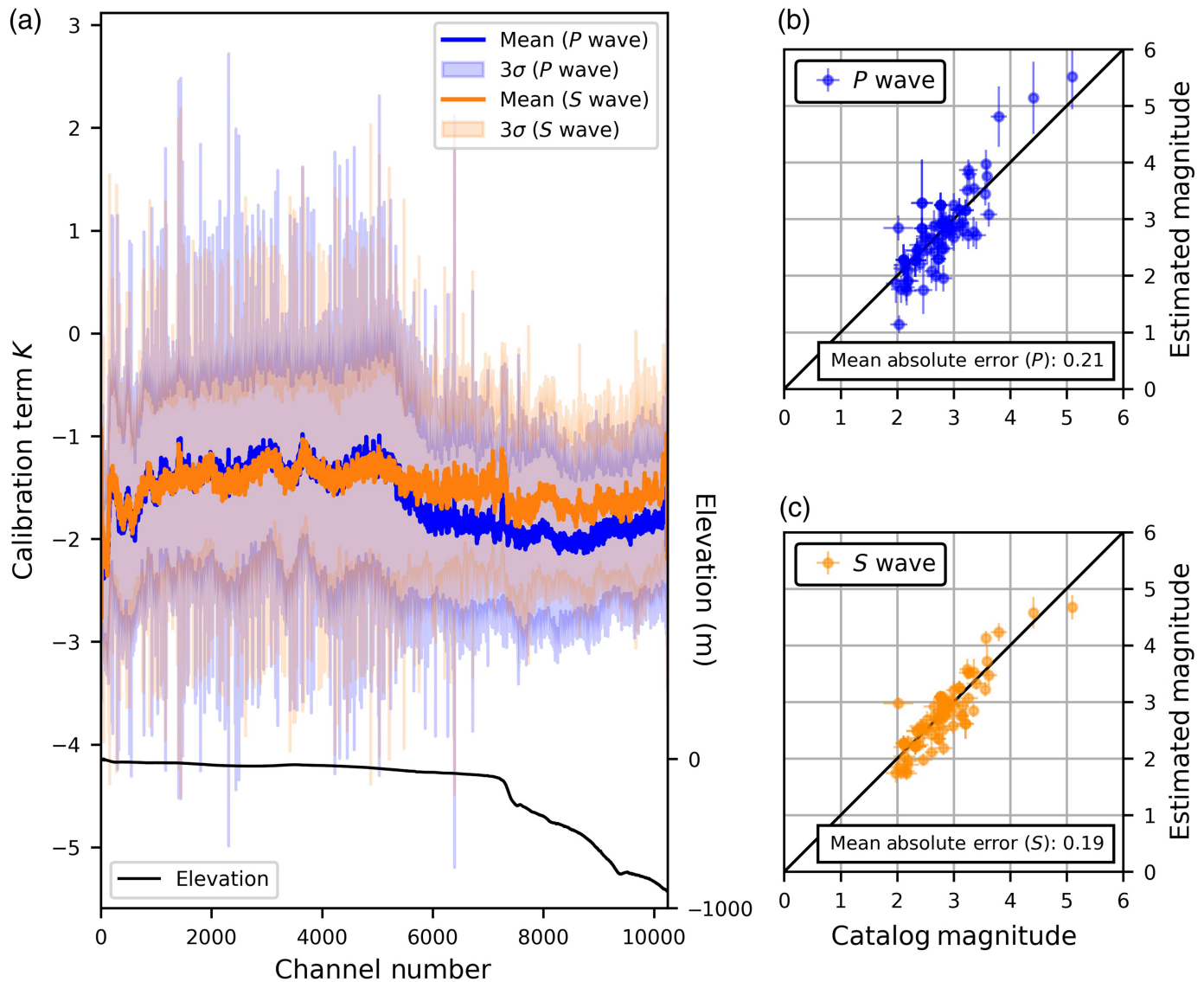
converting deformation derived from DAS data to displacement and then estimate magnitude using locally calibrated empirical equations. Other methods, for example, using low-frequency strain amplitudes (Nayak *et al.*, 2024) and coda waves (Gök *et al.*, 2024) are not suitable for EEW applications because they require longer waveforms.

Here, we used the base equation (equation 1) described in Yin, Zhu, *et al.* (2023) with local calibration for magnitude estimation, which is an empirical approach using DAS strain or strain-rate data directly. The main reasons behind this choice were its simplicity, which allows magnitude estimation in real time, similarity to the magnitude estimation method in EPIC, and good test results in our data set as shown subsequently.

In equation (1),  $E_i$  is the peak strain rate after the  $P$  or  $S$  arrival,  $D_i$  is the hypocentral distance,  $K_i$  is the calibration term at the  $i$ th channel, and  $M$  is the magnitude. The magnitude coefficient  $a$  and distance coefficient  $b$  in Yin, Zhu, *et al.* (2023) are 0.437 and 1.269, respectively, for  $P$  waves, 0.690 and 1.588 for  $S$  waves.

$$\log_{10}(E_i) = aM - b \log_{10}(D_i) + K_i. \quad (1)$$

We calibrated the  $K$  term for each channel using a subset of high-SNR events used in the training process of the new PhaseNet-DAS model (83 events). The peak strain rate within a 3 s window after the picked  $P$ - or  $S$ -wave arrival was used. Visualization of the calibration term across the DAS array in Figure 6a shows a strong correlation with bathymetry for



*P*-wave arrivals, while being relatively stable for *S* waves. Because the *K* term in equation (1) contains all the effects not explicitly accounted for in this equation, such as cable coupling condition, substrate type, earthquake radiation pattern, and directional sensitivity of DAS, it is difficult to interpret the correlation of the *K* term with water depth.

We calculated the median value of magnitude estimation from all channels, with the calibration terms. The results using both *P*- and *S*-wave peak strain rates were below 0.3 magnitude units (Fig. 6).

In the workflow, once an earthquake location is determined, hypocentral distance and peak strain rate within 3 s of each channel pick are used to calculate the magnitude using equation (1). Median magnitude estimation from available channels will be updated over time. In practice, the final magnitude estimation can be a weighted average of both *P*- and *S*-wave estimation with a higher weight for the latter.

The *P*-wave magnitude scaling in Figure 6b slightly deviates from one-to-one relationship between the estimated

**Figure 6.** Magnitude calibration and scaling results. The amplitude of the strain observed on all channels for all earthquakes is used to determine the calibration term *K* for each channel. (a) Variation in mean calibration term *K* along the length of the cable for the *P* (blue) and *S* wave (orange). The lighter blue and orange indicates three standard deviations range. The mean calibration term for each channel is used in equation (1) to estimate event magnitude. A comparison of the estimated and true magnitudes based on *P* and *S* waves is shown in panels (b) and (c), respectively. The overall mean absolute magnitude error is 0.25 for *P*-wave-based estimates and 0.16 for *S*-wave-based estimates. The error bars indicate the median absolute deviation (MAD) values. The color version of this figure is available only in the electronic edition.

magnitude and catalog magnitude. The deviation shows a slight trend of overestimation for larger events and underestimation for smaller events. This may suggest that the two coefficients *a* and *b* in equation (1) are not appropriate for our DAS data. This may be due to different regional average attenuation and the fact that most of the events used in the calibration were from a narrow azimuth range to the cable, which biased the

results because of the DAS array's directional sensitivity. To investigate this, we followed the workflow described in Yin, Zhu, *et al.* (2023) to calculate these coefficients from our own data set, subsequently recalculate  $K$  at each channel, and then re-estimate magnitudes for all events, as shown in Figure S6. Estimated magnitude with this new scaling does provide a better fit to the catalog magnitude. However, we only have a small data set to estimate the coefficients  $a$  and  $b$  compared to Yin, Zhu, *et al.* (2023), which could introduce an overfitting of data. Therefore, we chose to use the original coefficients.

We also explored the use of an empirical equation developed for strainmeter to directly map strain to magnitude (Barbour *et al.*, 2021). Because our DAS interrogator records data proportional to strain, we could also use this equation with our DAS data set without integration. A comparison of estimated and catalog magnitudes using this approach shows slightly lower mean absolute errors than using the DAS strain-rate scaling (equation 1) and is shown in Figure S7. The strainmeter coefficients derived by Barbour *et al.* (2021) use peak root mean squared strain from different gauges (component of strain inside the instrument), whereas DAS only measures axial strain in one direction. Based on the scaling relationship we obtained on our data set, we do not prefer one over the other and will keep testing both in the future when more data are available. Considering this study focuses on using DAS data and most interrogators output data in strain-rate units, we used the DAS strain-rate data derived scaling coefficients from Yin, Zhu, *et al.* (2023) and equation (1) in the following examples.

## EXAMPLE EVENTS

Before showing example earthquakes applying the proposed workflow to offshore events in Monterey Bay, we briefly summarized the workflow here. (1) A transfer-learning ML model scans continuous data to identify  $P$ - and  $S$ -first arrivals. (2) A weighted grid-search location method uses available phase picks to estimate the epicenter. (3) A calibrated empirical equation takes the peak strain rate to estimate the magnitude. We have observed more than 10 offshore earthquakes in Monterey Bay with a largest event of magnitude 2.4 ( $M_D$ , duration magnitude). We show the progression of the earthquakes for two example events occurring offshore and close to the cable. Although these events are small, in the case of larger events in these locations the DAS cable has the potential to increase warning times. The example events were analyzed retrospectively, with the data processed in moving windows.

Figure 7 shows the grid-search location results at 1.6–11.0 s after the earthquake origin time for an  $M$  2.4 event. Around 3 s after the origin time,  $\sim 3000$  channels identify  $P$ -wave arrivals. Because of the linear geometry of this closest section of the cable, the location result at 3.0 s is not well constrained. However, the location estimate quickly improves around 4.0 s when the  $P$ -wave moveout along a curved portion of the cable becomes available. This constrains the preferred earthquake location in

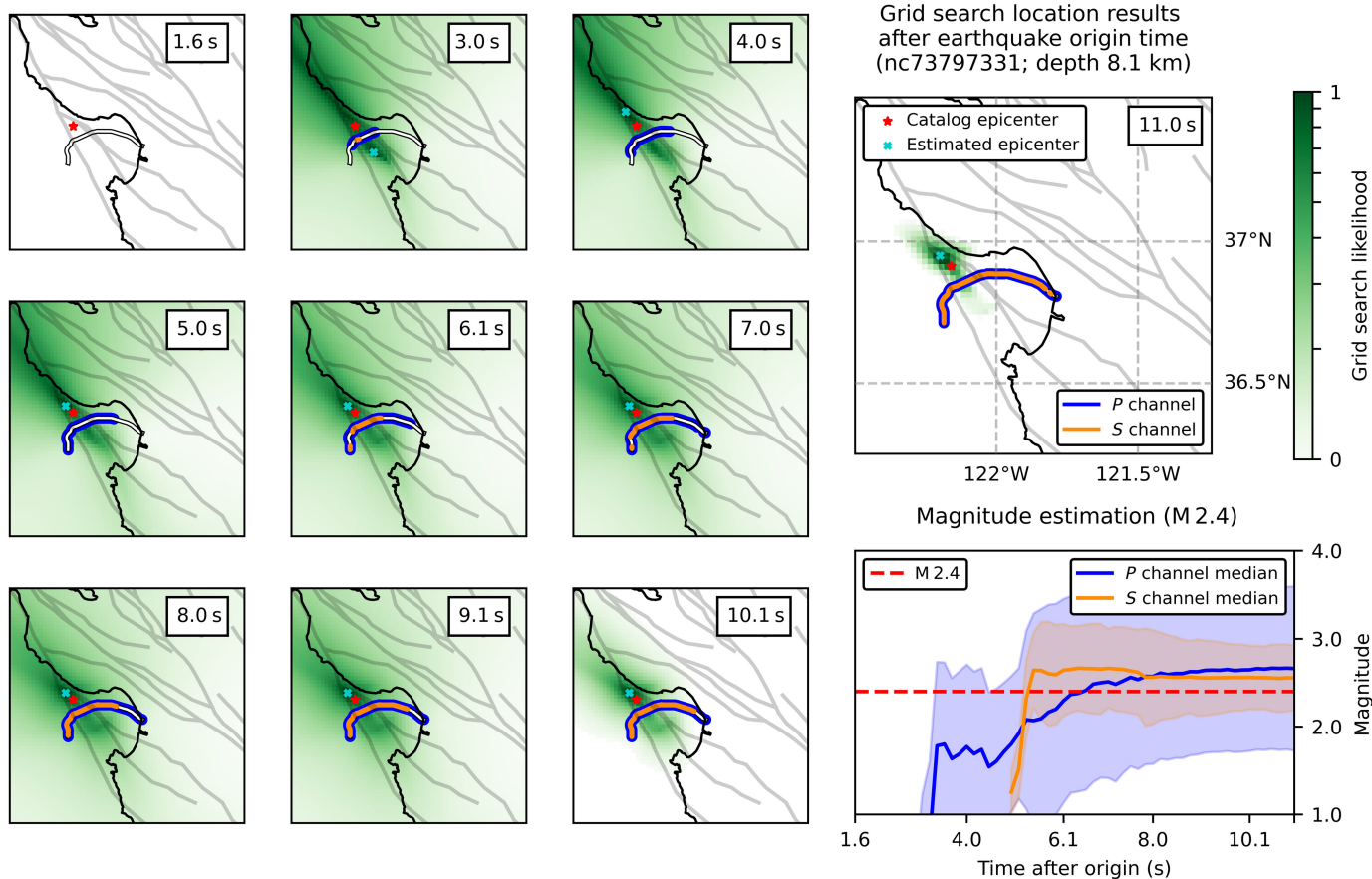
the north side of the cable. The grid-search likelihood is plotted with a logarithmic scale for better visualization. The actual values are much more concentrated around the maximum cyan cross. In this case, even before the  $S$  waves arrive, the location is close to the USGS catalog location with a location error of  $\sim 10$  km. Because of the weighting scheme for the picks and the iterative grid-search approach, we can see that the location converges stably over time to the catalog location. The final location error was  $\sim 5.4$  km. The magnitude estimates significantly improve and become more stable after 5.0 s with a  $\sim 0.2$  magnitude units difference compared to the USGS catalog magnitude. There are two other factors that may affect the magnitude estimation. (1) Directional sensitivity of the DAS measurement, which makes the first triggered linear section exhibit smaller amplitude for this earthquake than is typical. (2) The early contribution of channels at deeper water depths, which usually have higher SNR. We also conducted a similar analysis for this event, using the original PhaseNet-DAS model for phase picking instead, as illustrated in Figures S4 and S5.

Figure 8 shows the results for another  $M$  2.0 ( $M_D$ ) event, which was located “inside” the arc of this DAS array. Similar to the previous example, in the first few seconds,  $P$  arrivals were identified in a segment with a more linear geometry, causing ambiguity in the location. After the  $P$  waves reach the end of the cable, the first  $S$  waves have arrived (at 6.1 s), which helps constrain the location ( $\sim 4.8$  km location error). The underestimation ( $\sim 0.8$  units of magnitude) of the magnitude from  $P$  waves (including after the location stabilizes around 6.1 s) may be due to a lack of sensitivity in the DAS measurement. Some of the channels are also missing  $S$ -wave picks, likely because this is a relatively small event. We visually checked the waveforms and found that data from the shallow part of the cable are quite noisy. However, these inconsistent  $S$  picks do not affect the convergence of the location results because lower weights were assigned to these low-quality picks.

Overall, the proposed method worked well for the offshore events we have recorded in Monterey Bay. They served as proof of concept for the ability of earthquake detection using an individual offshore DAS array.

## DISCUSSION

We showed that an offshore DAS array alone can improve earthquake detection for the purpose of EEW, serving as a sentry for offshore fault zones, which are often outside the effective range of onshore seismic networks. In addition to California, other regions including Japan, Mexico, and Taiwan with operational EEW systems delivering public alerts would benefit from offshore DAS arrays allowing faster event detection and characterization. Regions that are still testing or planning for EEW systems should consider the possibility of adding offshore DAS arrays to the networks. This does not only apply to other regions such as Chile, Türkiye, and the Canadian west coast with offshore seismic hazard, but also



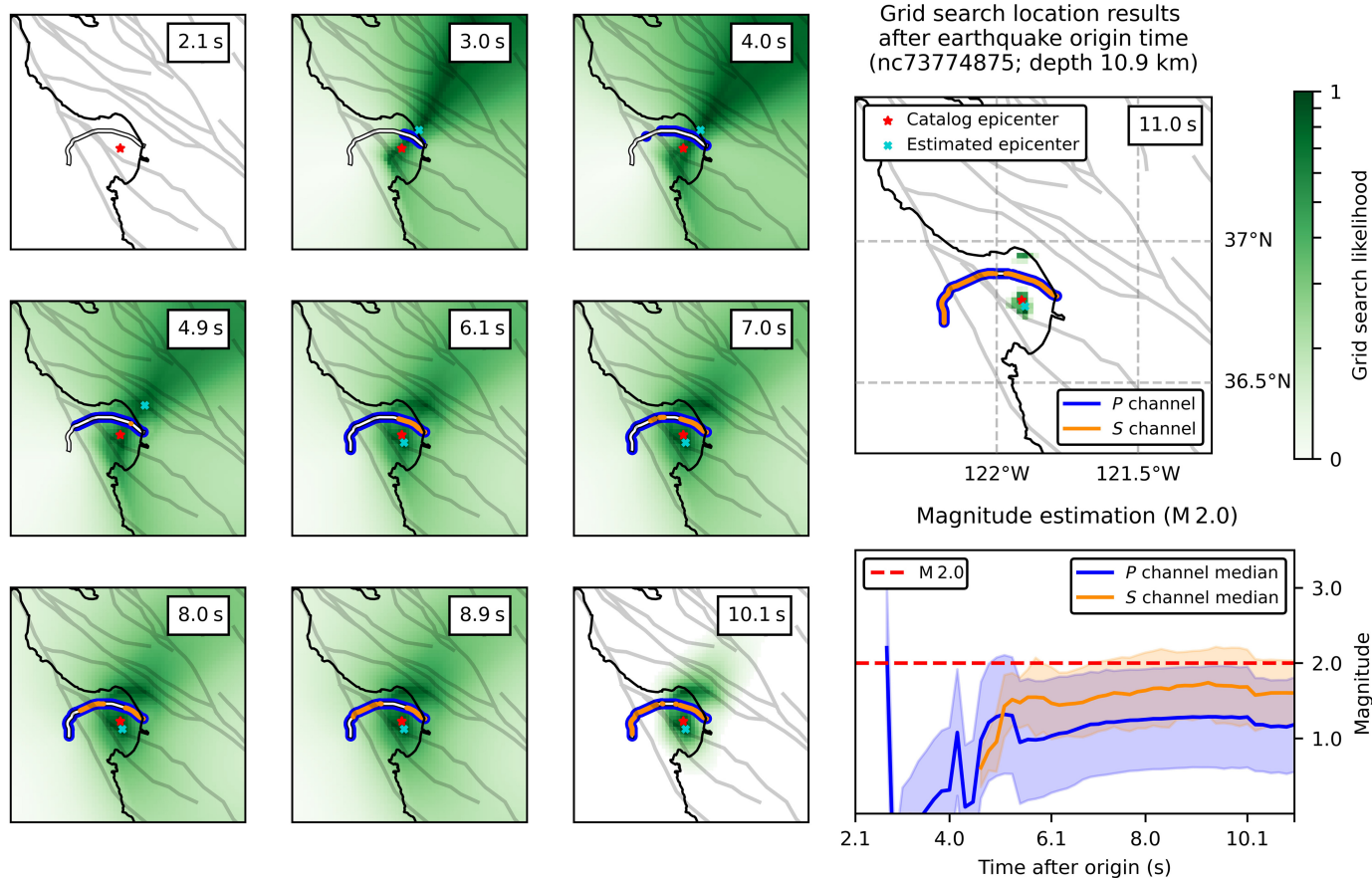
for regions such as Nepal where a fiber-optics DAS network may be more cost efficient than a high-quality modern broadband seismic network. Our proposed workflow can easily be adapted for a new cable with the pretrained PhaseNet-DAS model, calibrated magnitude estimation scaling, and the grid-search location algorithm.

As shown in the examples, the curved geometry of the MARS cable helps to constrain the earthquake location. Cables with linear geometry will encounter location ambiguity. A sensitivity test similar to the one shown in Figure 5 can facilitate the initial evaluation of the DAS array's geometry for earthquake detection and location. The sensitivity test can further be used to estimate additional warning time in the region, when the DAS array detects earthquakes faster than on-land networks. To do this, we need to determine how much location error we are willing to tolerate when we issue the first alert. Here, we set a location error threshold of 20 km. When a grid point on the time-dependent location sensitivity test map has less than 20 km location error, we declare an earthquake is detected and would issue the first alert. We can compare this DAS-detection time to the earliest detection EPIC algorithm can make using current ShakeAlert stations. The minimum requirement for the EPIC algorithm to issue an alert is that four stations have identified *P*-wave arrivals associated to the same earthquake. Therefore, we calculated the theoretical travel time for the *P* wave generated to reach the fourth

**Figure 7.** Detection performance for an offshore **M** 2.4 earthquake. Snapshots of the grid-search location results at different times after the earthquake origin time are shown in map view. The darker-green color represents higher likelihoods. The cyan cross marks the grid point with maximum likelihood and the red star marks the earthquake epicenter from the USGS catalog. The blue and orange colors on the MARS cable show DAS channels that have *P*- (blue) and *S*- (orange) arrival picks from the SeaFOAM PhaseNet-DAS model at that time. The lower right panel shows the time evolution of magnitude estimation using median value from available channels for *P* and *S* waves. The color version of this figure is available only in the electronic edition.

ShakeAlert station. By comparing the DAS and four-station EPIC detection times, we can estimate the additional warning time. Figure 9 shows the additional warning time for earthquakes in the Monterey Bay region with the MARS cable. When we assume that all the available ShakeAlert stations trigger and EPIC locates the earthquake perfectly, we still obtain 2–6 s additional warning time for earthquakes that happen in the offshore SGF zone when we make use of the MARS cable.

As pointed out by the ShakeAlert status and performance review (Lux *et al.*, 2024), the Mendocino triple junction region offshore Northern California is a particularly challenging area for the ShakeAlert system. As one of the most seismically active regions in California, it produced the recent 2021  $M_w$  6.1 and 6.0 Petrolia sequence, as well as the 20 December 2022  $M_w$  6.4



Ferndale sequence (Yoon and Shelly, 2024), which caused substantial damage in Humboldt County including two casualties (Stein *et al.*, 2023). Most recently, the 5 December 2024  $M_w$  7.0 earthquake occurred offshore Cape Mendocino, which was widely felt and triggered the ShakeAlert system, along with the U.S. tsunami warning system. However, due to the geometry limitation of onshore ShakeAlert stations (Fig. 9), it is difficult to constrain the locations of some offshore earthquakes. Both ShakeAlert's finite-fault EEW algorithm FinDer (Böse *et al.*, 2023; fault-specific templates) and the point-source EEW algorithm EPIC (Williamson *et al.*, 2023; Bayesian approach in earthquake location) are adding specific methods to improve the ShakeAlert performance in this region. Adding a submarine DAS cable to the existing land-based seismic network could greatly increase the offshore detection capacity. We conducted the same warning time calculation assuming a hypothetical  $\sim 200$  km linear cable extending westward offshore (Fig. 9b). Based on this cable geometry with the  $\sim 20$  km location error threshold, we can expect up to 20 s of additional warning time for events happening in regions near the cable and further offshore. Current state-of-art DAS interrogators can reach around 200 km distance but may be limited by repeaters along the cables.

The empirical magnitude scaling method works well but may be affected by the cable orientation relative to the locations of expected seismicity. Especially in our case, most of

**Figure 8.** Detection performance for an offshore  $M$  2.0 earthquake. Same legend as Figure 7. The color version of this figure is available only in the electronic edition.

the calibration events come from the SAF zone and are located on one side of the array. This may cause a bias that leads to the underestimation in the offshore examples. With time, more earthquakes in the Monterey Bay region will be detected with the cable and we will be able to resolve this bias should it exist.

The next step in the development of real-time EEW algorithms using the DAS data is to optimize the algorithms for real-time implementation and evaluate the performance including latency in data transmission and processing. Currently, data from all channels with 200 Hz are being streamed in real time to BSL. Estimated packet latency from the processing unit on site to our EEW server at the BSL is around 7–8 ms, which does not include the latency in the data acquisition process. The calculation time for the algorithm will be strongly dependent on the optimization of the algorithms and will be discussed in follow-up studies.

Another technical issue worth mentioning is the limits of dynamic range of DAS data (van den Ende *et al.*, 2024). DAS data will “clip” or saturate when the local strain or strain-rate measurement is too large and phase cycle skipping occurs. Strong ground motion may produce abrupt phase

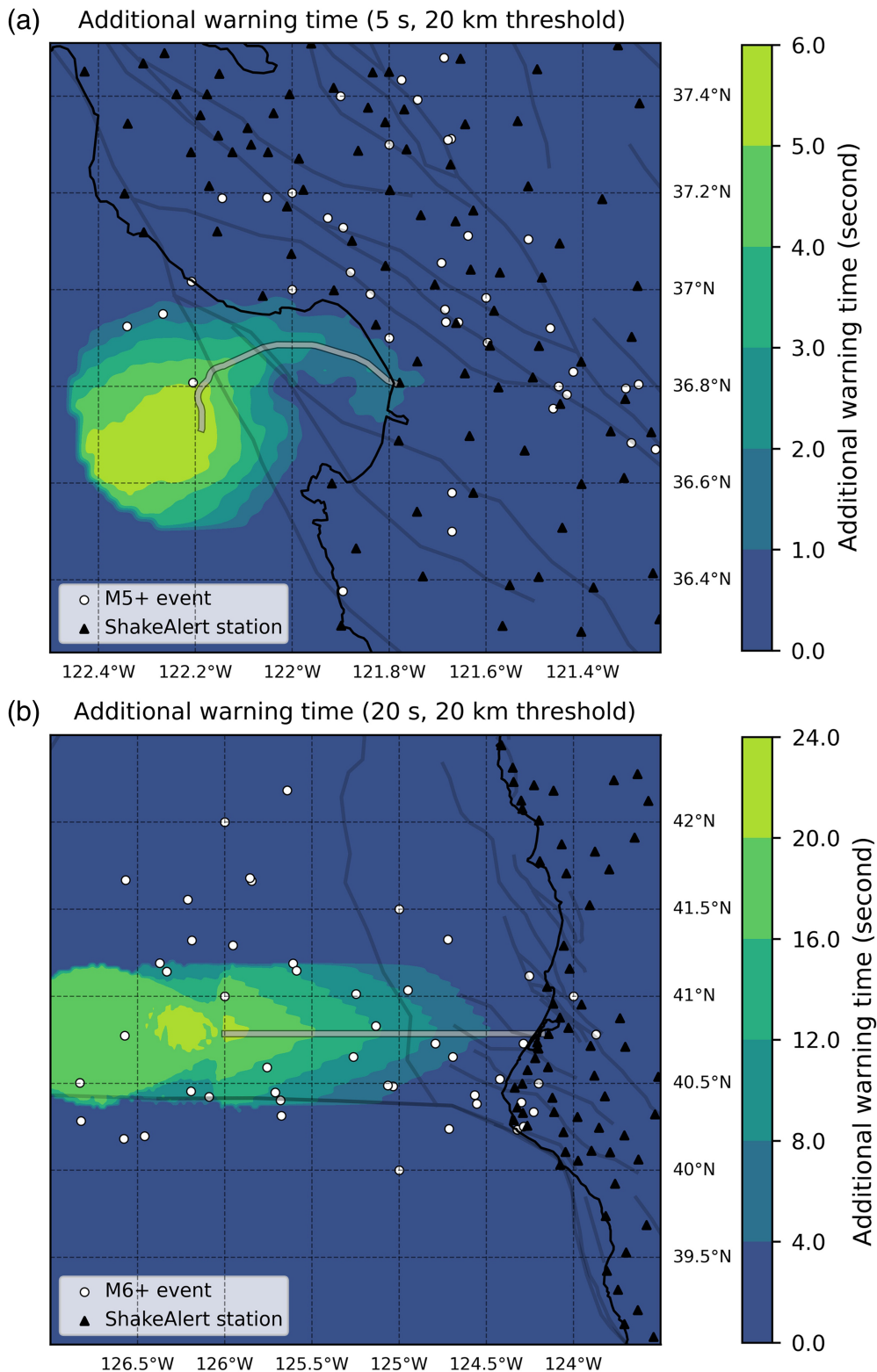


**Figure 9.** Additional earthquake early warning time provided by offshore DAS cables. The additional warning time is calculated for each grid point based on the location sensitivity map for the two cable geometries. We assume that an alert can be issued when the location error from the DAS-based detection drops below a threshold of 20 km. We compare this to the time it would take for the *P* wave to reach the fourth ShakeAlert station. The additional warning time is then the difference between these two times. (a) Additional warning time for events happening in the region around the MARS cable, and (b) results for a hypothetical cable located offshore near the Mendocino triple junction, a region where most offshore California earthquakes take place. The color version of this figure is available only in the electronic edition.

changes between two laser pulses that are more than  $2\pi$ , which cause the DAS record to clip. Recent studies like [Katakami \*et al.\* \(2024\)](#) provided possible solutions using corrections from coda normalization theory. We have not yet recorded an earthquake with strong ground motions on the SeaFOAM cable to explore this issue, but more studies on this limitation and potential technical solutions need to be developed ([van den Ende \*et al.\*, 2024](#)).

Other future potential for integrating DAS data into other EEW algorithms lies in the array nature of DAS. DAS's dense spatial sampling capability may be particularly valuable for finite source EEW algorithms like FinDer ([Böse \*et al.\*, 2012](#)), when the cable is located near the faults of interest. A DAS cable deployed along the fault may be able to trace the rupture, and is therefore more appropriate for a finite-fault source assumption. In addition, it is worth mentioning observations of detailed ground motion using DAS also opens the discussion of applications in ground-motion-based EEW algorithms such as PLUM (Propagation of Local Undamped Motion; [Hoshiba and Aoki, 2015](#)). DAS can record wavefield with high-spatial resolution around to provide detailed ground-motion information.

We envision future integration of this algorithm into the existing EPIC algorithm, essentially integrating data from onshore seismic stations with the offshore DAS array. This will require further research on both the operation side and the algorithm side. GPU

is needed to process real-time data using the PhaseNet-DAS model. The trade-off between detection speed and detection accuracy needs to be evaluated. The examples shown in this article are using all the DAS channels, which require a large volume of data to be processed in real time. Techniques such as channel selection, stacking, and data decimation may be helpful for reducing the data volume without lowering the earthquake detection accuracy. Finally, a decision module will be needed if we want to combine the outputs from the DAS array with the traditional network. To determine just how much warning time will be gained for offshore events, the next step is to start processing the data in real time.

## CONCLUSION

We developed a complete workflow for using a seafloor DAS array to detect earthquakes in real time. The workflow contains a locally retrained ML model for phase picking, an iterative grid search for earthquake location, and a locally calibrated empirical equation to estimate earthquake magnitude. With examples from offshore earthquakes in the SGF system, we show that the workflow is robust in phase picking, earthquake location, and magnitude estimation. It can potentially improve the performance of the current ShakeAlert EEW system in this region, with up to 6 s of additional warning time. Our workflow can be applied to other DAS arrays and provide estimation of the benefits such as additional EEW warning time in the region. We anticipate integrating this workflow into ShakeAlert's EPIC algorithm in the near future to enhance offshore EEW in California.

## DATA AND RESOURCES

Figure 1 was drawn using PyGMT available at <https://www.pygmt.org/v0.4.0>, a wrapper around Generic Mapping Tools version 6 (GMT6; Wessel *et al.*, 2019), with bathymetry data from National Centers for Environmental Information (2018). The earthquakes shown in figure are from U.S. Geological Survey (USGS) at <https://www.usgs.gov/programs/earthquake-hazards/earthquakes> and the International Seismological Centre-Global Earthquake Model (ISC-GEM) Catalog (Di Giacomo *et al.*, 2018). All the distributed acoustic sensing (DAS) data shown in this article are from the SeaFOAM project described in Romanowicz *et al.* (2023). All websites were last accessed in August 2024. The supplemental material includes detailed explanations of the machine learning (ML) model training process and performance evaluation, along with videos corresponding to Figures 3 and 7.

## DECLARATION OF COMPETING INTERESTS

The authors acknowledge that there are no conflicts of interest recorded.

## ACKNOWLEDGMENTS

This work is supported by National Science Foundation (NSF) Grant Number OCE-2023301 and California Governor's Office of Emergency Services, Agreement Number A211007522. The authors thank Barbara

Romanowicz for her guidance and support throughout the project as the principle investigator of the SeaFOAM project at UC Berkeley Seismological Laboratory (BSL); the authors thank Knute Brekke, Ivan Henson, Julien Marty, Doug Neuhauser, Brian Pardini, Stephen Thompson, Junli Zhang, Stephane Zuzlewski, Martin Karrenbach, and Victor Yartsev for their technical support. The authors thank Utpal Kumar, Angela Lux, Savvas Marcou, Nate Lindsey, and Amy Williamson for helpful discussions. The authors thank the editors and two anonymous reviewers for their helpful comments.

## REFERENCES

- Allen, R. (1982). Automatic phase pickers: Their present use and future prospects, *Bull. Seismol. Soc. Am.* **72**, no. 6B, S225–S242.
- Allen, R. M., and D. Melgar (2019). Earthquake early warning: Advances, scientific challenges, and societal needs, *Annu. Rev. Earth Planet. Sci.* **47**, 361–388.
- Atterholt, J., Z. Zhan, and Y. Yang (2022). Fault zone imaging with distributed acoustic sensing: Body-to-surface wave scattering, *J. Geophys. Res.* **127**, no. 11, e2022JB025052, doi: [10.1029/2022JB025052](https://doi.org/10.1029/2022JB025052).
- Barbour, A. J., J. O. Langbein, and N. S. Farghal (2021). Earthquake magnitudes from dynamic strain, *Bull. Seismol. Soc. Am.* **111**, no. 3, 1325–1346.
- Begnaud, M., K. McNally, D. Stakes, and V. Gallardo (2000). A crustal velocity model for locating earthquakes in Monterey Bay, California, *Bull. Seismol. Soc. Am.* **90**, no. 6, 1391–1408.
- Biondi, E., X. Wang, E. F. Williams, and Z. Zhan (2023). Geolocalization of large-scale das channels using a GPS-tracked moving vehicle, *Seismol. Res. Lett.* **94**, no. 1, 318–330.
- Böse, M., J. Andrews, R. Hartog, and C. Felizardo (2023). Performance and next-generation development of the finite-fault rupture detector (finder) within the united states west coast shakealert warning system, *Bull. Seismol. Soc. Am.* **113**, no. 2, 648–663.
- Böse, M., T. H. Heaton, and E. Hauksson (2012). Real-time finite fault rupture detector (finder) for large earthquakes, *Geophys. J. Int.* **191**, no. 2, 803–812.
- Bozzi, E., N. P. Agostinetti, A. Fichtner, S. Klaasen, A. Ugalde, B. Biondi, S. Yuan, T. Dahm, M. Isken, P. Paitz, *et al.* (2024). Modelling uncertainty in p-wave arrival-times retrieved from das data: Case-studies from 15 fibre optic cables, *Geophys. J. Int.* **239**, no. 3, 1928–1942.
- Capdeville, Y., and A. Sladen (2024). Das sensitivity to heterogeneity scales much smaller than the minimum wavelength, *Seismica* **3**, no. 1, doi: [10.26443/seismica.v3i1.1007](https://doi.org/10.26443/seismica.v3i1.1007).
- Di Giacomo, D., E. R. Engdahl, and D. A. Storchak (2018). The ISC-GEM earthquake catalogue (1904–2014): Status after the extension project, *Earth Syst. Sci. Data* **10**, no. 4, 1877–1899, doi: [10.31905/D808B825](https://doi.org/10.31905/D808B825).
- Cheng, F., B. Chi, N. J. Lindsey, T. C. Dawe, and J. B. Ajo-Franklin (2021). Utilizing distributed acoustic sensing and ocean bottom fiber optic cables for submarine structural characterization, *Sci. Rep.* **11**, no. 1, 5613.
- Chung, A. I., I. Henson, and R. M. Allen (2019). Optimizing earthquake early warning performance: Elarms-3, *Seismol. Res. Lett.* **90**, no. 2A, 727–743.
- Farghal, N. S., J. K. Saunders, and G. A. Parker (2022). The potential of using fiber optic distributed acoustic sensing (das) in earthquake early warning applications, *Bull. Seismol. Soc. Am.* **112**, no. 3, 1416–1435.

- Field, E. H., G. P. Biasi, P. Bird, T. E. Dawson, K. R. Felzer, D. D. Jackson, K. M. Johnson, T. H. Jordan, C. Madden, A. J. Michael, *et al.* (2015). Long-term time-dependent probabilities for the third uniform California earthquake rupture forecast (ucerf3), *Bull. Seismol. Soc. Am.* **105**, no. 2A, 511–543.
- Gök, R., W. R. Walter, J. Barno, C. Downie, R. J. Mellors, K. Mayeda, J. Roman-Nieves, D. Templeton, and J. Ajo-Franklin (2024). Reliable earthquake source parameters using distributed acoustic sensing data derived from coda envelopes, *Seismol. Res. Lett.* **95**, no. 4, 2208–2220.
- Graham, S., and W. Dickinson (1978). Evidence for 115 kilometers of right slip on the san Gregorio-Hosgri fault trend, *Science* **199**, no. 4325, 179–181.
- Hoshiya, M., and S. Aoki (2015). Numerical shake prediction for earthquake early warning: Data assimilation, real-time shake mapping, and simulation of wave propagation, *Bull. Seismol. Soc. Am.* **105**, no. 3, 1324–1338.
- Hudson, T. S., A. Stork, J. B. Muir, and A. Fichtner (2024). Unlocking das amplitude information through coherency coupling quantification, *EarthArXiv*, doi: [10.31223/X5V13N](https://doi.org/10.31223/X5V13N).
- Hui Lai, V., K. M. Hodgkinson, R. W. Porritt, and R. Mellors (2024). Toward a metadata standard for distributed acoustic sensing (DAS) data collection, *Seismol. Res. Lett.* **95**, 1986–1999.
- Johnson, S. Y., J. T. Watt, S. R. Hartwell, and J. W. Kluesner (2018). Neotectonics of the big sur bend, san Gregorio-Hosgri fault system, central California, *Tectonics* **37**, no. 7, 1930–1954.
- Kanazawa, T., K. Uehira, M. Mochizuki, T. Shinbo, H. Fujimoto, S. Noguchi, T. Kunugi, K. Shiomi, S. Aoi, T. Matsumoto, *et al.* (2016). *S-net Project, Cabled Observation Network for Earthquakes and Tsunamis*, Suboptic, Dubai.
- Katakami, S., S. Noda, M. Korenaga, E. Araki, N. Takahashi, and N. Iwata (2024). Potential of earthquake strong motion observation utilizing a linear estimation method for phase cycle skipping in distributed acoustic sensing, *J. Geophys. Res.* **129**, no. 1, e2023JB027327, doi: [10.1029/2023JB027327](https://doi.org/10.1029/2023JB027327).
- Kohler, M. D., D. E. Smith, J. Andrews, A. I. Chung, R. Hartog, I. Henson, D. D. Given, R. de Groot, and S. Guiwits (2020). Earthquake early warning ShakeAlert 2.0: Public rollout, *Seismol. Res. Lett.* **91**, no. 3, 1763–1775.
- Kuhnz, L., K. Buck, C. Lovera, S. Litvin, P. Whaling, and J. Barry (2020). Potential impacts of the monterey accelerated research system (mars) cable on the seabed and benthic faunal assemblages 2020, *MBNMS Permit Report*, 56 pp., doi: [10.13140/RG.2.2.12907.57122](https://doi.org/10.13140/RG.2.2.12907.57122).
- LeCun, Y., Y. Bengio, and G. Hinton (2015). Deep learning, *Nature* **521**, no. 7553, 436–444.
- Li, Z., Z. Shen, Y. Yang, E. Williams, X. Wang, and Z. Zhan (2021). Rapid response to the 2019 ridgecrest earthquake with distributed acoustic sensing, *AGU Adv.* **2**, no. 2, e2021AV000395, doi: [10.1029/2021AV000395](https://doi.org/10.1029/2021AV000395).
- Lindsey, N. J., and E. R. Martin (2021). Fiber-optic seismology, *Annu. Rev. Earth Planet. Sci.* **49**, no. 1, 309–336.
- Lindsey, N. J., T. C. Dawe, and J. B. Ajo-Franklin (2019). Illuminating seafloor faults and ocean dynamics with dark fiber distributed acoustic sensing, *Science* **366**, no. 6469, 1103–1107.
- Lindsey, N. J., H. Rademacher, and J. B. Ajo-Franklin (2020). On the broadband instrument response of fiber-optic das arrays, *J. Geophys. Res.* **125**, no. 2, e2019JB018145, doi: [10.1029/2019JB018145](https://doi.org/10.1029/2019JB018145).
- Lior, I., E. D. Mercerat, D. Rivet, A. Sladen, and J.-P. Ampuero (2022). Imaging an underwater basin and its resonance modes using optical fiber distributed acoustic sensing, *Seismol. Res. Lett.* **93**, no. 3, 1573–1584.
- Lior, I., D. Rivet, J.-P. Ampuero, A. Sladen, S. Barrientos, R. Sánchez-Olavarría, G. A. Villarroel Opazo, and J. A. Bustamante Prado (2023). Magnitude estimation and ground motion prediction to harness fiber optic distributed acoustic sensing for earthquake early warning, *Sci. Rep.* **13**, no. 1, 424.
- Lior, I., A. Sladen, D. Mercerat, J.-P. Ampuero, D. Rivet, and S. Sambolian (2021). Strain to ground motion conversion of distributed acoustic sensing data for earthquake magnitude and stress drop determination, *Solid Earth* **12**, no. 6, 1421–1442.
- Lior, I., A. Sladen, D. Rivet, J.-P. Ampuero, Y. Hello, C. Becerril, H. F. Martins, P. Lamare, C. Jestin, S. Tsagkli, *et al.* (2021). On the detection capabilities of underwater distributed acoustic sensing. *J. Geophys. Res.* **126**, no. 3, e2020JB020925, doi: [10.1029/2020JB020925](https://doi.org/10.1029/2020JB020925).
- Lomax, A. (2005). A reanalysis of the hypocentral location and related observations for the great 1906 California earthquake, *Bull. Seismol. Soc. Am.* **95**, no. 3, 861–877.
- Lux, A. I., D. Smith, M. Böse, J. J. McGuire, J. K. Saunders, M. Huynh, I. Stubailo, J. Andrews, G. Lotto, B. Crowell, *et al.* (2024). Status and performance of the ShakeAlert earthquake early warning system: 2019–2023, *Bull. Seismol. Soc. Am.* **114**, 3041–3062.
- Matsumoto, H., E. Araki, T. Kimura, G. Fujie, K. Shiraishi, T. Tonegawa, K. Obana, R. Arai, Y. Kaiho, Y. Nakamura, *et al.* (2021). Detection of hydroacoustic signals on a fiber-optic submarine cable, *Sci. Rep.* **11**, no. 1, 2797.
- National Centers for Environmental Information (2018). NOAA NOS Estuarine bathymetry - Monterey Bay (P080), National Centers for Environmental Information, NOAA, doi: [10.7289/V5639N1Q](https://doi.org/10.7289/V5639N1Q).
- Nayak, A., J. Correa, and J. Ajo-Franklin (2024). Seismic magnitude estimation using low-frequency strain amplitudes recorded by das arrays at far-field distances, *Bull. Seismol. Soc. Am.* **114**, no. 4, 1818–1838.
- Netanel, M., A. S. Eisermann, and A. Ziv (2021). Off-network earthquake location by earthquake early warning systems: Methodology and validation, *Bull. Seismol. Soc. Am.* **111**, no. 6, 3090–3102.
- Reinsch, T., T. Thurley, and P. Jousset (2017). On the mechanical coupling of a fiber optic cable used for distributed acoustic/vibration sensing applications—A theoretical consideration, *Meas. Sci. Technol.* **28**, no. 12, 127003.
- Romanowicz, B., R. Allen, K. Brekke, L.-W. Chen, Y. Gou, I. Henson, J. Marty, D. Neuhauser, B. Pardini, T. Taira, *et al.* (2023). Seafoam: A year-long das deployment in Monterey bay, California, *Seismol. Res. Lett.* **94**, no. 5, 2348–2359.
- Romanowicz, B., D. Stakes, R. Uhrhammer, P. McGill, D. Neuhauser, T. Ramirez, and D. Dolenc (2003). The MOBB experiment: A prototype permanent off-shore ocean bottom broadband station, *Eos Trans. AGU* **84**, no. 34, 325–332.
- Simpson, G. D., S. C. Thompson, J. S. Noller, and W. R. Lettis (1997). The northern san gregorio fault zone: Evidence for the timing of late holocene earthquakes near seal cove, California, *Bull. Seismol. Soc. Am.* **87**, no. 5, 1158–1170.
- Singh, S., Y. Capdeville, and H. Igel (2020). Correcting wavefield gradients for the effects of local small-scale heterogeneities, *Geophys. J. Int.* **220**, no. 2, 996–1011.

- Sladen, A., D. Rivet, J. P. Ampuero, L. De Barros, Y. Hello, G. Calbris, and P. Lamare (2019). Distributed sensing of earthquakes and ocean-solid earth interactions on seafloor telecom cables, *Nat. Commun.* **10**, no. 1, 5777.
- Stein, R. S., S. Toda, C. Rollins, and V. Sevilgen (2023). December 2022 California earthquake ruptured unknown fault: An analysis, *Temblor*, doi: [10.32858/temblor.294](https://doi.org/10.32858/temblor.294).
- Trabattoni, A., F. Biagioli, C. Strumia, M. van den Ende, F. Scotto di Uccio, G. Festa, D. Rivet, A. Sladen, J. P. Ampuero, J.-P. Métaxian, *et al.* (2023). From strain to displacement: using deformation to enhance distributed acoustic sensing applications, *Geophys. J. Int.* **235**, no. 3, 2372–2384.
- van den Ende, M., A. Trabattoni, M. Baillet, and D. Rivet (2024). An analysis of the dynamic range of distributed acoustic sensing for earthquake early warning, *EarthArXiv*, doi: [10.31223/X5KH5R](https://doi.org/10.31223/X5KH5R).
- Wessel, P., J. F. Luis, L. A. Uieda, R. Scharroo, F. Wobbe, W. H. Smith, and D. Tian (2019). The generic mapping tools version 6, *Geochem. Geophys. Geosys.* **20**, no. 11, 5556–5564.
- Williams, E. F., A. Ugalde, H. F. Martins, C. E. Becerril, J. Callies, M. Claret, M. R. Fernandez-Ruiz, M. Gonzalez-Herraez, S. Martin-Lopez, J. L. Pelegri, *et al.* (2023). Fiber-optic observations of internal waves and tides, *J. Geophys. Res.* **128**, no. 9, e2023JC019980, doi: [10.1029/2023JC019980](https://doi.org/10.1029/2023JC019980).
- Williamson, A., A. Lux, and R. Allen (2023). Improving out of network earthquake locations using prior seismicity for use in earthquake early warning, *Bull. Seismol. Soc. Am.* **113**, no. 2, 664–675.
- Wills, C. J., R. Weldon, and W. A. Bryant (2007). Appendix a: California fault parameters for the national seismic hazard map and working group on California earthquake probabilities, *U.S. Geol. Surv. Open-File Rept. 2007-1437A*.
- Xiao, H., Z. J. Spica, J. Li, and Z. Zhan (2024). Detection of earthquake infragravity and tsunami waves with underwater distributed acoustic sensing, *Geophys. Res. Lett.* **51**, no. 2, e2023GL106767, doi: [10.1029/2023GL106767](https://doi.org/10.1029/2023GL106767).
- Yang, Y., Z. Zhan, Z. Shen, and J. Atterholt (2022). Fault zone imaging with distributed acoustic sensing: Surface-to-surface wave scattering, *J. Geophys. Res.* **127**, no. 6, e2022JB024329, doi: [10.1029/2022JB024329](https://doi.org/10.1029/2022JB024329).
- Yin, J., M. A. Soto, J. Ramirez, V. Kamalov, W. Zhu, A. Husker, and Z. Zhan (2023). Real-data testing of distributed acoustic sensing for offshore earthquake early warning, *Seism. Record* **3**, no. 4, 269–277.
- Yin, J., W. Zhu, J. Li, E. Biondi, Y. Miao, Z. J. Spica, L. Viens, M. Shinohara, S. Ide, K. Mochizuki, *et al.* (2023). Earthquake magnitude with DAS: A transferable data-based scaling relation, *Geophys. Res. Lett.* **50**, no. 10, e2023GL103045, doi: [10.1029/2023GL103045](https://doi.org/10.1029/2023GL103045).
- Yoon, C. E., and D. R. Shelly (2024). Distinct yet adjacent earthquake sequences near the Mendocino triple junction: 20 December 2021 m w 6.1 and 6.0 Petrolia, and 20 December 2022 m w 6.4 Ferndale, *Seism. Record* **4**, no. 1, 81–92.
- Zhan, Z. (2020). Distributed acoustic sensing turns fiber-optic cables into sensitive seismic antennas, *Seismol. Res. Lett.* **91**, no. 1, 1–15.
- Zhu, W., and G. C. Beroza (2019). Phasenet: A deep-neural-network-based seismic arrival-time picking method, *Geophys. J. Int.* **216**, no. 1, 261–273.
- Zhu, W., E. Biondi, J. Li, J. Yin, Z. E. Ross, and Z. Zhan (2023). Seismic arrival-time picking on distributed acoustic sensing data using semi-supervised learning, *Nat. Commun.* **14**, no. 1, 8192.
- Zhu, W., I. W. McBrearty, S. M. Mousavi, W. L. Ellsworth, and G. C. Beroza (2022). Earthquake phase association using a Bayesian Gaussian mixture model, *J. Geophys. Res.* **127**, no. 5, e2021JB023249, doi: [10.1029/2021JB023249](https://doi.org/10.1029/2021JB023249).
- Ziv, A., A. S. Eisermann, O. Volk, and I. Zbeda (2024, 05). Introducing ViDA3, an earthquake early warning algorithm for offshore hypocenter determination using onshore seismic networks, *Bull. Seismol. Soc. Am.* **114**, no. 5, 2446–2456.

---

Manuscript received 27 September 2024

Published online 30 January 2025